This is an *Accepted Manuscript*, which has been through the RSC Publishing peer review process and has been accepted for publication.

Accepted Manuscripts are published online shortly after acceptance, which is prior to technical editing, formatting and proof reading. This free service from RSC Publishing allows authors to make their results available to the community, in citable form, before publication of the edited article. This *Accepted Manuscript* will be replaced by the edited and formatted *Advance Article* as soon as this is available.

To cite this manuscript please use its permanent Digital Object Identifier (DOI®), which is identical for all formats of publication.

More information about *Accepted Manuscripts* can be found in the **Information for Authors**.

Please note that technical editing may introduce minor changes to the text and/or graphics contained in the manuscript submitted by the author(s) which may alter content, and that the standard **Terms & Conditions** and the **ethical guidelines** that apply to the journal are still applicable. In no event shall the RSC be held responsible for any errors or omissions in these *Accepted Manuscript* manuscripts or any consequences arising from the use of any information contained in them.

Design of new electrode materials for Li-ion and Na-ion batteries from the *Bloedite* mineral Na$_2$Mg(SO$_4$)$_2$·4H$_2$O

Marine Reynaud,[a] Gwenaëlle Rousse,[b] Artem M. Abakumov,[c] Moulay T. Sougrati,[d] Gustaaf Van Tendeloo,[c] Jean-Noël Chotard,[a] Jean-Marie Tarascon[a,*]

[a] Laboratoire de Réactivité et Chimie des Solides, Université de Picardie Jules Verne, CNRS UMR 7314, 33 rue Saint Leu, 80039 Amiens, France.

[b] Institut de Minéralogie et de Physique des Milieux Condensés, Université Pierre et Marie Curie (UPMC Univ. Paris 06), CNRS UMR 7590, 4 Place Jussieu, 75252 Paris Cedex 05, France.

[c] Electron Microscopy for Materials Science, University of Antwerp, Groenenborgerlaan 171, B-2020 Antwerp, Belgium.

[d] Institut Charles Gerhardt – Laboratoire des Agrégats, Interfaces et Matériaux pour l'Energie, Université de Montpellier II, CNRS UMR 5253, 34095 Montpellier Cedex 5, France.

* Corresponding author: E-mail: jean-marie.tarascon@sc.u-picardie.fr

Table of contents

Starting from the *Bloedite* mineral, we prepared two new electrode materials, $Na_2Fe(SO_4)_2.4H_2O$ and $Na_2Fe(SO_4)_2$, which present high redox potentials of 3.6 V *vs.* lithium and 3.3-3.4 V *vs.* sodium.
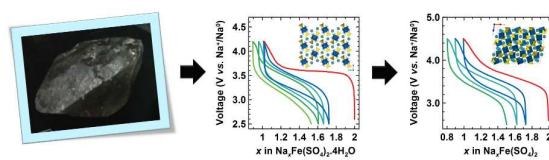
Abstract

Mineralogy offers a large database to search for Li- or Na-based compounds having suitable structural features for acting as electrode materials, $LiFePO_4$ being one example. Here we further explore this avenue and report on the electrochemical properties of the *Bloedite*-type compounds $Na_2M(SO_4)_2 \cdot 4H_2O$ (M = Mg, Fe, Co, Ni, Zn) and their dehydrated phases $Na_2M(SO_4)_2$ (M = Fe, Co), whose structure has been solved *via* complementary Synchrotron X-ray diffraction, neutron powder diffraction and transmission electron microscopy. Among these compounds, the hydrated and anhydrous iron-based phases show electrochemical activity with the reversible uptake of 1 Na^+ or 1 Li^+ at high voltages of ~3.3 V vs. Na^+/Na^0 and ~3.6 V *vs.* Li^+/Li^0, respectively. Although the reversible capacities remain lower than 100 mAh/g, we hope this work would stress further the importance of mineralogy as a source of inspiration for designing eco-efficient electrode materials.

Introduction

Lithium-ion batteries have been essential to the development of portable electronic devices for the past two decades. This technology is now being integrated into larger volume applications, such as electrical transportation and stationary electrochemical energy storage. Besides, fears of lithium reserves have rekindled a growing interest in Na-ion batteries as a possible alternative to Li-ion batteries for mass storage applications. The penalty in energy density associated to the use of sodium (*e.g.* higher mass, lower potential) is overcompensated by its lower cost owing to its abundance on Earth. This, combined with the feasibility of using aluminum negative current collector, leads to a cheaper kWh for the Na-ion technology as compared to the Li-ion one. Nevertheless, whatever the targeted market, both lithium and sodium technologies still need to be improved in order to match the energy density, security and sustainability requirements dictated by upcoming automotive and grids applications. Meeting such challenges sorely requests innovation in designing new materials.

Several strategies can be pursued to efficiently design new attractive materials. One relies on high-throughput materials computation to identify the "magic phase composition" having both high voltage and high capacity,[1–4] but success is still limited. Another one, mainly pursued by experimental chemists, consists in browsing through the structures of known compounds (*e.g.* already synthesized phases, minerals) to spot families of materials having attractive structural features for ions transport. We opted for the second option, making use of the about 4000 identified mineral species on Earth to design new electrode materials.

Besides, previous works had showed that sulfate compounds generally present higher potentials (*e.g. NASICON* $Fe_2(SO_4)_3$ (3.6 V *vs.* Li^+/Li^0),[5,6] *Tavorite* $LiFeSO_4F$ (3.6 V

vs. Li$^+$/Li^0),[7] *layered* LiFeSO$_4$OH (3.6 V *vs.* Li$^+$/Li^0),[8] *Marinite* Li$_2$Fe(SO$_4$)$_2$ (3.83 V *vs.* Li$^+$/Li^0),[9,10] *Maxwellite* NaFeSO$_4$F (3.5 V *vs.* Na$^+$/Na^0),[11] *Triplite* LiFeSO$_4$F (3.9 V *vs.* Li$^+$/Li^0)[12,13]) than other polyanionic electrode materials, including the current benchmark LiFePO$_4$ (3.45 V *vs.* Li$^+$/Li^0)[14]; this is the reason why we specifically focused on sulfate minerals.

Among them, the *Bloedite* Na$_2$M(SO$_4$)$_2$.4H$_2$O (M = Mg, Zn), whose reported structure presents wide pathways in which alkaline ions lay, captured our attention. Such mineral compounds have been widely studied since the 1940's, and their synthesis was swiftly extended to the preparation of nickel, cobalt and iron analogues.[15–27] Later, Cot showed the possibility of removing the structural water from these materials, and the author speculated about the formation of several polymorphs of anhydrous phases Na$_2$M(SO$_4$)$_2$ (M = Fe, Co, Ni, Zn).[18] Except for the zinc system for which a crystal structure has been reported,[28] none of these water-free phases was further investigated.

Herein we revisit these hydrated and dehydrated phases, solve the crystal structure of anhydrous phases α-Na$_2$M(SO$_4$)$_2$ (M = Co, Fe) and report on the electrochemical properties of both water-containing and water-free iron-based compounds *versus* both lithium and sodium.

Experimental section

Syntheses: Several procedures have been employed in the past to prepare the Na$_2$M(SO$_4$)$_2$·4H$_2$O (M = Mg, Zn, Co, Ni) phases. Here, we chose first a simple process, inspired from natural sedimentation, which consists in slowly evaporating an equimolar solution of commercial sodium sulfate Na$_2$SO$_4$ and metal sulfate heptahydrate MSO$_4$·7H$_2$O at temperatures ranging from 20°C to 90°C. Then, we experienced that the targeted phases

were also easily obtained by precipitating the solutions of sulfate precursors in ethanol. Alternatively, we equally succeeded in preparing the $Na_2M(SO_4)_2 \cdot 4H_2O$ phases by ball-milling (Spex 8000M®) for 20 minutes equimolar amounts of the two aforementioned precursors. Whatever the synthetic route used, these hydrated phases form accordingly to the following reaction:

$$Na_2SO_4 + M^{II}SO_4 \cdot 7H_2O \rightarrow Na_2M^{II}(SO_4)_2 \cdot 4H_2O + 3H_2O$$

Given the great aptitude of the Fe^{II}-based precursors to oxidize, the iron analogue $Na_2Fe(SO_4)_2 \cdot 4H_2O$ was prepared using similar routes but provided the reaction was done under inert conditions (*i.e.* under argon, in presence of degassed solvents, and/or by adding ascorbic acid).

α-$Na_2M(SO_4)_2$ phases (M = Co, Fe) were obtained by slowly dehydrating the corresponding $Na_2M(SO_4)_2 \cdot 4H_2O$ compounds at temperatures ranging between 120 and 260°C either under air (M = Co) or under nitrogen (M = Fe). The cobalt phase α-$Na_2Co(SO_4)_2$ could also be obtained from a stoichiometric mixture of Na_2SO_4 and $CoSO_4$ pressed into a pellet and heated under air above 400°C for few hours.

Structural analyses: Various complementary techniques were used:

X-Ray Diffraction (XRD). Powder patterns were recorded using a Bruker D8 diffractometer equipped with a Vantec detector and a Co Kα radiation ($\lambda_{K\alpha1}$ = 1.78897 Å, $\lambda_{K\alpha2}$ = 1.79285 Å), operating at 40 kV/40 mA. High temperature XRD experiments were carried out with the same diffractometer, equipped with an Anton Paar HTK 1200 furnace. For these experiments, the powder samples were heated under air or under nitrogen flow from room temperature to 600°C with a ramp of 12°C/min, and a delay of five minutes was observed at each temperature before running the 110-min long scan.

High-resolution Synchrotron X-Ray powder Diffraction. Data were collected for the cobalt-based system at the CRISTAL beamline at SOLEIL Synchrotron (Saint-Aubin, France) with a wavelength of 0.6681 Å. The $Na_2Co(SO_4)_2 \cdot 4H_2O$ powder sample was filled in a 0.7-mm diameter quartz capillary opened at one end. The formation of the α-$Na_2Co(SO_4)_2$ phase was followed by recording the X-ray patterns while heating the hydrated sample using a Cyberstar hot-gas blower.

Neutron Powder Diffraction (NPD). Powder patterns were recorded at room temperature on the high resolution D2B diffractometer at the Institut Laue Langevin (ILL, Grenoble, France), using a wavelength of 1.594 Å.

The X-ray and Neutron powder diffraction patterns were refined using the Rietveld method as implemented in the FullProf program.[29,30] The structures were standardized using the STRUCTURE TIDY program,[31] and they were drawn and examined with the help of the VESTA visualization program.[32]

Transmission Electron Microscopy. The α-$Na_2Co(SO_4)_2$ sample was prepared in an argon-filled glove box by crushing the crystals in dry hexane and depositing drops of suspension onto holey carbon grid. The grid was transported to the microscope under Ar atmosphere. Selected Area Electron Diffraction (SAED) patterns and EDX spectra were obtained with a Tecnai G2 electron microscope operated at 200 kV equipped with an EDAX attachment. SAED patterns of α-$Na_2Co(SO_4)_2$ were taken with a very weak and widely spread electron beam. In these conditions the material almost did not suffer from the electron beam damage and allowed obtaining tilt series of the SAED patterns, which could be used for a reconstruction of the 3D reciprocal lattice.

Mössbauer spectroscopy: [57]Fe Mössbauer spectra were recorded in transmission geometry in the constant acceleration mode using a [57]Co(Rh) source with nominal activity

of 925 MBq. The velocity scale ($\pm$ 4 mm.s^{-1}) was calibrated at room temperature with an α-Fe foil standard. The absorbers were prepared from 20 to 50 mg of powder. The hyperfine parameters δ (isomer shift) and ΔE_q (quadrupole splitting) were determined by fitting Lorentzian lines to the experimental data using the FullHam program. The isomer shifts values are calculated with respect to that of α-Fe.

Infrared spectroscopy (FTIR): For IR measurements, the samples were mixed with KBr powder before sustaining a 10-ton pressure for one minute to form a 13 mm-diameter pellet. Spectra were collected in the 5000-500 cm^{-1} wavenumber range using a Nicolet Avatar 370 DTGS spectrometer in transmission mode.

TGA: The stability of the samples was investigated by thermogravimetric analyses (TGA) and differential scanning calorimetry (DSC) coupled with mass spectrometry (MS) in the temperature range 20-700°C (heating rate: 10°C/min) under argon using a STA-449C Jupiter unit (Netzsch). The mass spectrometer was a quadrupole QMS 403 Aëolos with stainless-steel capillary and a secondary-electron multiplier detector (Channeltron).

Electrochemical characterization: Electrochemical tests *versus* lithium and sodium were carried out in Swagelok®-type cells. The working composite electrodes were typically made by ball-milling for 20 minutes (Spex® 8000) under Ar atmosphere the powdered active material with Super P carbon black in a 70:30%wt ratio. Unless otherwise specified, the cells were assembled in an argon-filled glove box, using the above working electrode material as a positive electrode and a Li-metal (or Na-metal) disc as the negative electrode, separated by two Whatman® GF/D borosilicate glass fiber sheets saturated with 1M LiClO$_4$ (or NaClO$_4$) in propylene carbonate (PC) as the electrolyte. Usual cathode loading was

9-12 mg.cm^{-2} of powder composite per cell. Galvanostatic charge/discharge tests were conducted at 20°C using a Mac-Pile system (BioLogic, S.A.), and the cells were typically cycled at a rate of 1 alkaline ion (Li$^+$ or Na$^+$) exchanged per 50 h.

For the *ex situ* XRD experiment described in the main text, several Na // NaClO$_4$ in PC // Na$_2$Fe(SO$_4$)$_2$·4H$_2$O cells were launched and stopped at different states of charge and discharge (*i.e.* different amount of Na$^+$ removed from or re-inserted in the active material). The positive electrode material was then washed with PC, before being dried under primary vacuum for one hour, and finally being X-ray under argon using a special sample holder equipped with a X-ray transparent beryllium window.

Results and discussion

The titled compounds Na$_2$*M*(SO$_4$)$_2$·4H$_2$O (*M* = Mg, Zn, Ni, Co, Fe) prepared as described in the Experimental Section were obtained as single phases. Their X-Ray Diffraction (XRD) patterns could be fully indexed on the basis of a monoclinic cell (space group *P*2$_1$/*c*) as previously reported for the *Bloedite*-type compounds.[24] Combining both Synchrotron X-ray diffraction and Neutron Powder Diffraction data of the highly-crystallized Na$_2$Co(SO$_4$)$_2$·4H$_2$O phase enabled to refine hydrogen positions without any constraints. The results of the refinements are presented in Table 1 and Figure 1 for the cobalt compound and in Supporting Information Tables SI-1 to SI4 and Figure SI-1 to SI-5 for the Mg, Zn, Ni and Fe samples.

The *Bloedite* structure is built upon isolated units made of one *M*O$_2$(OH$_2$)$_4$ octahedron and two SO$_4$ tetrahedra (insets Figure 1). The distance between two metals is above 5 Å, and as a result the Co(SO$_4$)$_2$(H$_2$O)$_4$ units are rather spaced one from another (selected distances and angles for Na$_2$Co(SO$_4$)$_2$.4H$_2$O are given in Supporting Information

Table SI-5). The sodium atoms sit in large channels and are coordinated by six oxygen atoms to form NaO_6 octahedra which are linked two by two through edges, forming isolated Na_2O_{10} bi-octahedra.

To explore the feasibility of sodium transport in these large channels, we studied the electrochemical properties of these hydrated compounds $Na_2M(SO_4)_2 \cdot 4H_2O$ (M = Mg, Zn, Ni, Co, Fe). The iron-based phase was the only one to show electrochemical activity against both lithium and sodium, once the proper electrolyte was used. Initial attempts to use classical Li(Na)-PF_6 based electrolytes failed as a drastic voltage drop appeared when nearly ~0.4 Na^+ ion was extracted from the material (data not shown here). We believe that at this stage of Na^+ ion removal, structural water becomes more labile and reacts with $LiPF_6$ leading to its decomposition into PF_5 + HF, with the latter decomposing our electrode material; hence our motivation to employ PF_6^--free electrolytes such as $LiClO_4$ in PC or LiTFSI in EC/DMC. We found that $Na_2Fe(SO_4)_2 \cdot 4H_2O$ can successfully cycle *versus* either Li or Na metal using $LiClO_4$ and $NaClO_4$-based PC electrolytes, respectively (Figure 2). Whatever the nature of the negative electrode (Li or Na), the first charge whose amplitude nearly approaches one sodium is flat. This contrasts with the following discharge and subsequent charge/discharge curves which show an S-type shape. This phenomenon is highlighted when plotting the derivatives (dx/dV): they show a sharp peak for the first charge, which becomes broader for the successive cycles. From both potential-composition and derivative curves, one can deduce that the electrochemical activity after the first charge is centered near 3.6 V *versus* Li^+/Li^0 and 3.3 V *versus* Na^+/Na^0. These potentials are higher than the ones of $LiFePO_4$ (3.45 V *vs.* Li^+/Li^0)[14] and compare with other sulfate compounds.[5–9,11–13] Note that the 300 mV difference between the potential of the lithium half-cell and the one of the sodium half-cell falls within the range of what is expected

between the two alkaline redox couples (-3.04 V and -2.71 V *vs.* SHE respectively). Last, the shift to the left of the voltage-composition curves suggests a progressive solvent decomposition upon charging, with this effect being more pronounced for Na- than Li-based cells. This assumption was supported by the yellowish coloration of the recovered separator after cycling. Attempts to alleviate this issue, through electrolyte purification or electrolyte additives, have not yet positively materialized.

To grasp insights into the evolution of the voltage-composition curves from flat to S-type between the first charge and the subsequent discharge, *ex situ* XRD were carried out. For this purpose, Na // $Na_2Fe(SO_4)_2 \cdot 4H_2O$ cells were assembled, stopped at different states of charge and discharge and the electrode recovered, washed and X-rayed. The collected diffraction patterns (Figure 3a) show the progressive amorphization of the active material $Na_xFe(SO_4)_2 \cdot 4H_2O$ upon charging. Such an amorphization is consistent with the onset of a S-type voltage/composition curve once the first charge is achieved. Featureless XRD patterns were equally obtained for chemically oxidized $NaFe(SO_4)_2 \cdot 4H_2O$ samples (Figure SI-6), which were prepared from the pristine $Na_2Fe(SO_4)_2 \cdot 4H_2O$ and using NO_2BF_4 in acetonitrile as oxidizing agent.

Mössbauer Spectroscopy was used to gain access to the changes in the local environment of Fe and its oxidation states upon sodium removal and uptake. The spectrum recorded for the pristine $Na_2Fe(SO_4)_2.4H_2O$ (bottom box of Figure 3b) is perfectly fitted using a single and narrow doublet of a Fe(II) in high-spin configuration, confirming that there is a unique iron site in the structure (Table 2). No trace of Fe(III) was detected, confirming the purity of the pristine phase $Na_2Fe(SO_4)_2 \cdot 4H_2O$ whatever the synthesis route employed. The Mössbauer spectrum of the sample recovered at the end of the first charge (middle box of Figure 3b) shows that iron is fully oxidized and the Fe(III) is in a high spin

configuration, but the large width of the signal suggests a distribution of iron environments, in agreement with the amorphous nature of the sample. The spectrum of the sample at the end of the first discharge presents the same kind of large signals typical of amorphous phases (upper box of Figure 3b), and one can note that the hyperfine parameters of the Fe(II) are different from the ones of the pristine phase, confirming again the change of the active material morphology.

To complete the characterization of the electrode material during the first charge-discharge cycle, we probed the presence of water by combining infra-red spectroscopy (Supporting Information Figure SI-7) and thermogravimetric analyses coupled to mass spectroscopy. These measurements confirmed the presence of four molecules of structural water in both the pristine phase $Na_2Fe(SO_4)_2\cdot4H_2O$ and the $NaFe(SO_4)_2\cdot4H_2O$ sample obtained through chemical oxidation, but, to our surprise, the electrode material recovered after the first charge conversely show no trace of water. After verifying that $Na_2Fe(SO_4)_2\cdot4H_2O$ does not dehydrate when submerged into the electrolyte during extended time, we concluded that the loss of the structural water of our electrode material occurs concurrently to the electrochemical sodium removal and the amorphization of the structure, these concurrent phenomena being traduced in the peculiar flat-like trace of the first charge.

At this stage, an obvious prolongation of this work was to prepare dehydrated $Na_2M(SO_4)_2$ phases to study their electrochemical behavior (theoretical specific capacity of ~91 mAh/g *versus* ~73 mAh/g for the hydrated phases). Cot had previously reported the existence of these anhydrous phases[18] but their structures were not solved, hence the need to prepare high purity and well crystallized samples. This called for an accurate understanding of the water removal process.

Thermogravimetric analyses coupled with mass-spectroscopy measurements confirmed the release of the four molecules water from $Na_2Fe(SO_4)_2 \cdot 4H_2O$ and $Na_2Co(SO_4)_2 \cdot 4H_2O$ between 120 and 250°C (Figure 4). To access the structural evolution of the hydrated phases upon water departure, we monitored its XRD evolution as a function of the heating temperature. As one can see in Figure 5, both iron and cobalt samples display a similar behavior during the water-loss process. The beginning of the dehydration is associated with a radical change of the XRD patterns (green patterns in Figure 5), from which we could identify a certain quantity of Na_2SO_4 and $MSO_4 . H_2O$ (M = Co or Fe) among other unknown phases. At the end of the dehydration, we observed the crystallization of a new phase whose pattern (shown in red in Figure 5) matches with the Debye-Scherrer pattern reported by Cot for α-$Na_2Co(SO_4)_2$.[18] ATG-MS and FTIR analyses on the recovered samples confirmed the removal of water (Supporting Information Figure SI-7). The nominal composition was confirmed by EDX analysis performed with a transmission electron microscope, using short times exposures to prevent the gradual loss of sodium. At this stage, it is worth mentioning that we also managed to prepare the α-$Na_2Co(SO_4)_2$ phase directly from a stoichiometric mixture of Na_2SO_4 and $CoSO_4$ heated above 400°C for a few hours, but all our attempts to stabilize the iron analogue α-$Na_2Fe(SO_4)_2$ from its anhydrous precursors failed. Moreover, despite many tries, this latter compound could not be obtained as a pure phase from $Na_2Fe(SO_4)_2 \cdot 4H_2O$, as an unidentified phase tended to grow in competition with the targeted one. However, by adjusting the dehydration conditions (temperature ramp, nitrogen flow, quantity of sample, etc), we were able to prepare samples which mainly contained the α-$Na_2Fe(SO_4)_2$ phase, so that we could probe its electrochemical behavior.

The structural determination of α-Na$_2$M(SO$_4$)$_2$ (M = Co, Fe) was carried on the cobalt-based compound because these samples were both better crystallized and less sensitive to oxidation upon air exposure, which makes them easier to handle. Synchrotron X-ray powder Diffraction data was collected at the CRISTAL beamline at SOLEIL (see Experimental Section). We first tried to refine the α-Na$_2$Co(SO$_4$)$_2$ pattern starting from the structure proposed for Na$_2$Zn(SO$_4$)$_2$ by Berg and Thorup.[28] This model led to acceptable Rietveld refinement of the main reflections, with the following parameters: S.G. *P2/n*, *a* = 8.9725(2) Å, *b* = 10.3834(2) Å, *c* = 15.0443(2) Å, β = 90.235(5)°, *V* = 1401.62(4) Å^3; however it did not allow to describe weak reflections, which could be attributed to the existence of a superstructure (Supporting Information Figure SI-8a). This assumption was confirmed with Neutron Powder Diffraction, performed on the D2B diffractometer at the Institut Laue Langevin. This technique provides better contrast between the different elements which constitute the phase, as with neutrons Co scatters less efficiently (b$_{Co}$ = 2.49 fm) whereas Na, S and O give strong contributions to the intensities of the neutron Bragg reflections (b$_{Na}$ = 3.63 fm, b$_S$ = 2.847 fm, b$_O$ = 5.803 fm). The Rietveld refinement of the high-resolution NPD pattern α-Na$_2$Co(SO$_4$)$_2$ using the Na$_2$Zn(SO$_4$)$_2$ model was poor, especially for reflections in the range 35 ≤ 2θ ≤ 60° (Supporting Information Figure SI-8b). This was an indication that α-Na$_2$Co(SO$_4$)$_2$ adopts a structural model different from the one reported for the Zn analogue,[28] with the main difference between both models not resting in the transition metal position, as the XRD refinement is acceptable, but rather in the Na, S and O distribution.

At this juncture, attempts to find the proper unit cell for α-Na$_2$Co(SO$_4$)$_2$ from complementary Synchrotron XRD and Neutron Powder Diffraction patterns were leading to numerous possibilities with cells having large volumes (2500-3000 Å^3). To sort out between these different options we performed Transmission Electron Microscopy (TEM).

Using very weak and widely spread electron beam, tilt series of the SAED patterns were collected and used for a reconstruction of the 3D reciprocal lattice. As seen in Figure 6a, the patterns present two groups of reflections with different intensities, confirming the existence of a superstructure. All bright reflections in the electron diffraction patterns could be indexed with the subcell derived from the $Na_2Zn(SO_4)_2$ model proposed by Berg and Thorup[28] and mentioned above. Indexation of the weaker reflections requires a new monoclinic supercell with the lattice vectors related to the vectors of the subcell as $\mathbf{a}_{super} = 2\mathbf{a}_{sub} + \mathbf{c}_{sub}$, $\mathbf{b}_{super} = -\mathbf{b}_{sub}$, $\mathbf{c}_{super} = \mathbf{a}_{sub} - \mathbf{c}_{sub}$. This leads to the supercell lattice parameters: $a_{super} \approx 23.3$ Å, $b_{super} \approx 10.3$ Å, $c_{super} \approx 17.4$ Å, $\beta \approx 99.0^{\circ}$, which corresponds to a cell volume three times larger than the subcell ($V_{super} \approx 4204$ Å^3 vs. $V_{sub} \approx 1402$ Å^3).

The Berg and Thorup's $Na_2Zn(SO_4)_2$ atomic positions were then transformed into this supercell, and the space group was determined to be $C2/c$. The Rietveld refinement of the Synchrotron XRD data using this model with soft constraints on the S-O distances of the sulfate group enabled to fit almost all weak superlattice reflections of the pattern (Figure 6b) (a few very weak reflections remain unindexed and may be attributed to a possible admixture). Then, this supercell was also checked against our neutron powder diffraction data, and it was found to perfectly match (Figure 6c). Finally, a joint Rietveld refinement was performed against both the Synchrotron XRD and the NPD data; the corresponding results are given in Figure 6 and Table 3, and selected distances are reported in Table SI-6.

The structure of α-$Na_2Co(SO_4)_2$ as determined above is illustrated in Figure 7. No obvious structural relation with its precursor $Na_2Co(SO_4)_2 \cdot 4H_2O$ phase seems to exist. The structure consists in a complicated arrangement of CoO_6 octahedra and SO_4 tetrahedra, resulting in a very large unit cell. In fact, CoO_6 octahedra and SO_4 tetrahedra are alternately connected either by corners and edges or by corners only, which gives rise to small chains

as shown in Figure 7c. Thus, each CoO_6 octahedron is linked to four SO_4 groups by vertices and shares an edge with a fifth SO_4 tetrahedron. As for the sulfate groups, they are connected either to two CoO_6 octahedra (through one corner and one edge) or to three different CoO_6 octahedra (through corners only); in both cases, the fourth oxygen of the SO_4 tetrahedra points to small cavities where the Na atoms sit. Overall, the main difference between the structure of α-$Na_2Co(SO_4)_2$ and the one reported for $Na_2Zn(SO_4)_2$[28] resides in the orientation of the SO_4 groups, which explains why the mismatch was barely noticeable from X-Ray Diffraction only but was much more obvious from Neutron Powder Diffraction.

The electrochemical activity of the α-$Na_2M(SO_4)_2$ phases were tested against both Na and Li negative electrodes. Similarly to what had been observed for the parent hydrated phase, no electrochemical activity could be detected for α-$Na_2Co(SO_4)_2$ up to 5 V, which corresponds to the electrochemical stability limit of our electrolyte. This contrasts with α-$Na_2Fe(SO_4)_2$ whose electrochemical activity is within the 2.5 – 4.5 V range (Figure 8). The voltage-composition traces indicate that almost one sodium can be extracted from the structure, out of which either nearly 0.7 lithium or sodium can then be reversibly re-inserted with again high experimental potentials centered around 3.6 V *vs.* Li^+/Li^0 and 3.4 V *vs.* Na^+/Na^0, respectively. The discharge capacities remain stable upon cycling but one should note, as for the Fe-based hydrated phase, that the curves are "walking to the left" as a result of a longer charge than discharge, and this effect is highly enhanced for sodium cells. We believe it is linked to electrolyte degradation issues that we have not yet mastered. At this point it is worth mentioning that the charge voltage profile for $Na_2Fe(SO_4)_2$ which shows an S-curve, differs from that of $Na_2Fe(SO_4)_2·4H_2O$ which exhibits a first flat-like, suggesting a different Na removal mechanism.

Conclusion

Through this study, we reported on the synthesis of *Bloedite*-type compounds $Na_2M(SO_4)_2 \cdot 4H_2O$ (M = Mg, Zn, Ni, Co, Fe) and of their dehydrated derivatives $Na_2M(SO_4)_2$ (M = Co and Fe) for which we have solved the complete structure for the first time. The iron-based phases are the only ones to show electrochemical activity, with the removal of nearly one sodium at high potentials of 3.6 V *vs.* Li^+/Li^0 or 3.3–3.4 V *vs.* Na^+/Na^0.

These Fe^{III+}/Fe^{II+} redox potentials exceed the benchmarked value of $LiFePO_4$ (3.45 V *vs.* Li^+/Li^0) and compare with the potentials reported for other sulfate-based electrode materials such as $Fe_2(SO_4)_3$, $LiFeSO_4F$ or $LiFeSO_4OH$. However the reversible capacities of the $Na_2Fe(SO_4)_2 \cdot nH_2O$ (n = 0, 4) compounds (below 100 mAh/g) make them of limited interest for practical electrode materials. Besides, these materials present a poor coulombic efficiency upon cycling which is more pronounced with Na-based electrolytes. Such an oxidation-driven electrolyte instability is not related to the eventual presence of water in our Fe-based compounds as it occurs whether our starting material is hydrated or not, but rather to an electrode-electrolyte incompatibility whose underlying mechanism has yet not being elucidated.

Overall, we have demonstrated that minerals form a rich structural database from which we can get inspiration to design-identify new insertion materials, but novelty does not always rhyme with practicality.

References

1. G. Ceder, presented at Collège de France, Paris, 2011, available at http://www.college-de-france.fr/site/jean-marie-tarascon/.
2. A. Jain, G. Hautier, C. J. Moore, S. P. Ong, C. C. Fischer, T. Mueller, K. A. Persson, and G. Ceder, *Computational Materials Science*, 2011, **50**, 2295–2310.
3. S. P. Ong, A. Jain, G. Hautier, M. Kocher, S. Cholia, D. Gunter, D. Bailey, D. Skinner, K. Persson, and G. Ceder, *The Materials Project*, available at http://materialsproject.org/.
4. G. Hautier, A. Jain, and S. Ong, *J. Mater. Sci.*, 2012, **47**, 7317–7340.
5. A. Manthiram and J. B. Goodenough, *Journal of Power Sources*, 1989, **26**, 403–408.
6. A. K. Padhi, K. S. Nanjundaswamy, C. Masquelier, and J. B. Goodenough, *J. Electrochem. Soc.*, 1997, **144**, 2581–2586.
7. N. Recham, J.-N. Chotard, L. Dupont, C. Delacourt, W. Walker, M. Armand, and J.-M. Tarascon, *Nature Mater.*, 2010, **9**, 68–74.
8. C. V. Subban, M. Ati, G. Rousse, A. M. Abakumov, G. Van Tendeloo, R. Janot, and J.-M. Tarascon, *J. Am. Chem. Soc.*, 2013.
9. M. Reynaud, M. Ati, B. C. Melot, M. T. Sougrati, G. Rousse, J.-N. Chotard, and J.-M. Tarascon, *Electrochem. Commun.*, 2012, **21**, 77–80.
10. M. Reynaud, G. Rousse, J.-N. Chotard, J. Rodríguez-Carvajal, and J.-M. Tarascon, *Inorganic Chemistry*, 2013, **52**, 10456–10466.
11. P. Barpanda, J.-N. Chotard, N. Recham, C. Delacourt, M. Ati, L. Dupont, M. Armand, and J.-M. Tarascon, *Inorg. Chem.*, 2010, **49**, 7401–7413.
12. P. Barpanda, M. Ati, B. C. Melot, G. Rousse, J.-N. Chotard, M.-L. Doublet, M. T. Sougrati, S. A. Corr, J.-C. Jumas, and J.-M. Tarascon, *Nature Mater.*, 2011, **10**, 772–779.
13. M. Ati, B. C. Melot, J.-N. Chotard, G. Rousse, M. Reynaud, and J.-M. Tarascon, *Electrochem. Commun.*, 2011, **13**, 1280–1283.
14. A. K. Padhi, K. S. Nanjundaswamy, and J. B. Goodenough, *J. Electrochem. Soc.*, 1997, **144**, 1188–1194.
15. C. Lauro, *Period. Mineral.*, 1940, **11**, 89–94.
16. I. M. Rumanova and G. I. Malitskaya, *Kristallografiya*, 1959.
17. M. Giglio, *Acta Crystallogr.*, 1958, **11**, 789–794.
18. L. Cot, *Rev. Chim. Min.*, 1969, **6**, 1041–1070.
19. S. Peytavin, G. Brun, J. Guillermet, L. Cot, and M. Maurin, *Spectrochim. Acta A*, 1972, **28**, 2005–2011.
20. V. I. Bukin and Y. Z. Nozik, *J. Struct. Chem.*, 1974, **15**, 616–619.
21. V. I. Bukin and Y. Z. Nozik, *Kristallografiya*, 1975, **20**, 293.
22. F. C. Hawthorne, *Can. Mineral*, 1985, **23**, 669–674.
23. C. Vizcayno and M. T. Garcia-Gonzalez, *Acta Crystallogr. C*, 1999, **C55**, 8–11.
24. D. Stoilova and M. Wildner, *J. Mol. Struct.*, 2004, **706**, 57–63.
25. M. E. Díaz de Vivar, S. Baggio, M. T. Garland, and R. Baggio, *Acta Crystallogr. E*, 2006, **62**, i196–i198.
26. M. E. Díaz de Vivar, S. Baggio, A. Ibáñez, and R. Baggio, *Acta Crystallogr. E*, 2008, **E64**, i30–i31.
27. M. Hudák, J. G. Díaz, and J. Kožíšek, *Acta Crystallogr. E*, 2008, **64**, i10–i10.
28. R. W. Berg and N. Thorup, *Inorg. Chem.*, 2005, **44**, 3485–3493.
29. J. Rodríguez-Carvajal, *Physica B*, 1993, **192**, 55–69.
29. J. Rodríguez-Carvajal, FullProf Suite, available at http://www.ill.eu/sites/fullprof/index.html.
31. L. M. Gelato and E. Parthé, *J. Appl. Crystallogr.*, 1987, **20**, 139–143.
32. K. Momma and F. Izumi, *J. Appl. Crystallogr.*, 2011, **44**, 1272–1276.

Tables

Table 1:

Crystallographic data and atomic positions of $Na_2Co(SO_4)_2.4H_2O$ deduced from a joint Rietveld refinement of SOLEIL Synchrotron X-ray diffraction (λ = 0.6681 Å) and ILL neutron diffraction (λ = 1.594 Å) data. Bond Valence Sum analysis (BVS) is also indicated.

			$Na_2Co(SO_4)_2.4H_2O$			
Space group P 2_1/c		χ^2 = 1.37		R_{Bragg} = 5.72 %	V = 498.18(5) Å^3	
a = 5.5356(4) Å		*b* = 8.2436(5) Å		*c* = 11.0978(6) Å	β = 100.356(5)°	
Atom	*Wyckoff site*	*x/a*	*y/b*	*z/c*	B_{iso} Å^2	*BVS*
Na	4*e*	0.1290(12)	0.0700(9)	0.3617(5)	0.99(15)	1.11(2)
Co	2*a*	0	0	0	0.31(6)	2.00(2)
S	4*e*	0.3701(9)	0.2879(5)	0.1361(4)	0.47(9)	5.93(9)
O1	4*e*	0.3462(15)	0.2704(12)	0.2676(9)	1.1(2)	2.13(4)
O2	4*e*	0.2026(15)	0.4151(12)	0.0789(9)	1.0(2)	2.04(4)
O3	4*e*	0.3148(15)	0.1319 (12)	0.0725(9)	0.9(2)	1.80(4)
O4	4*e*	0.6280(18)	0.3299(12)	0.1320(9)	1.0(2)	2.31(4)
O5	4*e*	0.1277(15)	0.5392(12)	0.3379(9)	0.8(2)	1.66(4)
O6	4*e*	0.1760(15)	0.7861(12)	0.0815(9)	0.9(2)	1.58(4)
H1	4*e*	0.230(9)	0.445(5)	0.321(4)	2.2(9)	0.93(3)
H2	4*e*	0.227(9)	0.636(5)	0.344(4)	3.2(9)	1.05(4)
H3	4*e*	0.683(9)	0.303(6)	0.359(5)	3.1(9)	1.03(3)
H4	4*e*	0.237(9)	0.719(6)	0.021(4)	3.2(9)	0.98(4)

Table 2:

Room temperature Mössbauer parameters for the pristine $Na_2Fe(SO_4)_2 \cdot 4H_2O$ and the electrode materials recovered at the end of the first charge and at the end of the first discharge. δ, ΔE_q and Γ are the isomer shift relative to metallic iron standard at room temperature, the quadrupole splitting and the line width, respectively.

		δ (mm/s)	ΔEq (mm/s)	Γ (mm/s)	%
$Na_2Fe(SO_4)_2 \cdot 4H_2O$ (pristine)	Fe(II)	1.25(1)	3.25(1)	0.27(1)	100
$NaFe(SO_4)_2 \cdot 4H_2O$ (end of first charge)	Fe(III)	0.42(1)	0.51(2)	0.49(3)	100
$Na_{1.7}Fe(SO_4)_2 \cdot 4H_2O$ (end of first discharge)	Fe(II)	1.15(2)	2.39(4)	0.66(7)	72(4)
	Fe(III)	0.42(1)	0.51(2)	0.49(3)	28(4)

Table 3:

Crystallographic data and atomic positions of α-$Na_2Co(SO_4)_2$ deduced from a joint Rietveld refinement of SOLEIL Synchrotron X-ray diffraction (λ = 0.6681 Å) and ILL neutron diffraction (λ = 1.594 Å) data. Bond Valence Sum analysis (BVS) is also indicated. Note that the S−O distances were controlled with soft constraints.

			α-$Na_2Co(SO_4)_2$			
Space group C 2/c	χ^2 = 3.26		R_{Bragg} = 5.49 %		V = 4121.4(6) Å³	
a = 23.262(2) Å	*b* = 10.3057(9) Å		*c* = 17.4047(15) Å		β = 98.972(6)°	
Atom	*Wyckoff site*	*x/a*	*y/b*	*z/c*	B_{iso} Å²	*BVS*
Co1	8*f*	0.4288(6)	0.1048(13)	0.0600(8)	1.41(10)	1.74(7)
Co2	8*f*	0.4002(6)	0.3842(14)	0.2728(9)	1.41(10)	1.90(8)
Co3	8*f*	0.2359(7)	0.1286(12)	0.1198(8)	1.41(10)	2.01(8)
Na1	4*e*	0	0.144(5)	¼	3.2(3)	0.83(4)
Na2	8*f*	0.1684(19)	0.340(3)	0.428(2)	3.2(3)	0.98(6)
Na3	8*f*	0.4007(17)	0.107(4)	0.396(2)	3.2(3)	0.93(5)
Na4	8*f*	0.0626(15)	0.118(4)	0.077(2)	3.2(3)	1.10(6)
Na5	8*f*	0.2392(16)	0.379(4)	0.234(2)	3.2(3)	1.08(7)
Na6	4*e*	0	0.589(5)	¼	3.2(3)	1.03(5)
Na7	8*f*	0.3365(18)	0.449(3)	0.072(3)	3.2(3)	0.64(5)
S1	8*f*	0.4735(8)	0.3789(18)	0.1246(10)	1.43(15)	6.3(3)
O11	8*f*	0.4763(15)	0.239(2)	0.1319(19)	1.55(6)	2.03(13)
O12	8*f*	0.0325(11)	0.074(3)	0.6431(18)	1.55(6)	2.17(14)
O13	8*f*	0.4438(14)	0.421(3)	0.0502(15)	1.55(6)	2.02(15)
O14	8*f*	0.4428(14)	0.433(3)	0.1843(17)	1.55(6)	1.99(17)
S2	8*f*	0.1901(8)	0.3780(17)	0.0249(10)	1.43(15)	5.9(3)
O21	8*f*	0.3531(13)	0.208(3)	0.0191(18)	1.55(6)	1.94(14)
O22	8*f*	0.1676(13)	0.506(3)	0.0388(17)	1.55(6)	1.91(15)
O23	8*f*	0.2109(14)	0.321(3)	0.1024(14)	1.55(6)	1.98(13)
O24	8*f*	0.2559(11)	0.106(4)	0.0089(18)	1.55(6)	1.97(14)
S3	8*f*	0.3619(8)	0.1042(17)	0.2144(10)	1.43(15)	5.9(3)
O31	8*f*	0.3143(13)	0.185(3)	0.1754(18)	1.55(6)	1.92(14)
O32	8*f*	0.3430(14)	0.010(3)	0.2692(16)	1.55(6)	1.79(15)
O33	8*f*	0.4077(12)	0.187(3)	0.2573(18)	1.55(6)	2.14(14)
O34	8*f*	0.3875(14)	0.031(2)	0.1552(16)	1.55(6)	1.80(14)
S4	8*f*	0.1818(8)	0.1047(17)	0.5879(10)	1.43(15)	6.1(3)
O41	8*f*	0.1579(14)	0.025(3)	0.0748(19)	1.55(6)	2.14(14)

O42	8*f*	0.2604(11)	0.424(3)	0.3706(19)	1.55(6)	2.15(15)
O43	8*f*	0.3511(13)	0.316(3)	0.3633(17)	1.55(6)	1.84(15)
O44	8*f*	0.1868(14)	0.179(4)	0.5185(15)	1.55(6)	1.80(15)
S5	8*f*	0.0047(8)	0.3694(17)	0.4150(10)	1.43(15)	6.0(3)
O51	8*f*	0.0108(14)	0.490(3)	0.1289(16)	1.55(6)	1.95(13)
O52	8*f*	0.0601(11)	0.391(3)	0.4641(17)	1.55(6)	2.02(14)
O53	8*f*	0.0393(13)	0.341(4)	0.0338(17)	1.55(6)	2.01(16)
O54	8*f*	0.0069(14)	0.261(3)	0.3636(17)	1.55(6)	1.99(16)
S6	8*f*	0.1624(8)	0.1104(17)	0.2667(11)	1.43(15)	6.1(3)
O61	8*f*	0.3246(15)	0.475(3)	0.2093(18)	1.55(6)	2.15(13)
O62	8*f*	0.1604(15)	0.186(4)	0.3374(16)	1.55(6)	1.81(15)
O63	8*f*	0.1073(11)	0.100(4)	0.2157(19)	1.55(6)	2.05(15)
O64	8*f*	0.2094(13)	0.160(3)	0.2279(18)	1.55(6)	2.05(16)

Figures

Figure 1:

Results of the joint Rietveld refinement of (a) the Synchrotron X-ray powder diffraction ($\lambda = 0.6681$ Å) and (b) the neutron powder diffraction ($\lambda = 1.594$ Å) patterns of $Na_2Co(SO_4)_2.4H_2O$. The green ticks represent the Bragg peak positions of the phase. The red crosses and the black line are the experimental and the simulated patterns, respectively. The difference between these two patterns is shown with the blue line. In inset: projections of the structure of $Na_2Co(SO_4)_2.4H_2O$ along the *a*-axis (top) and the *b*-axis (bottom). The $Co(SO_4)_2(H_2O)_4$ units are constituted of one blue CoO_6 octahedron linked two yellow SO_4 tetrahedra and four H_2O molecules; H atoms are displayed as small grey balls. Cyan spheres correspond to the Na atoms.
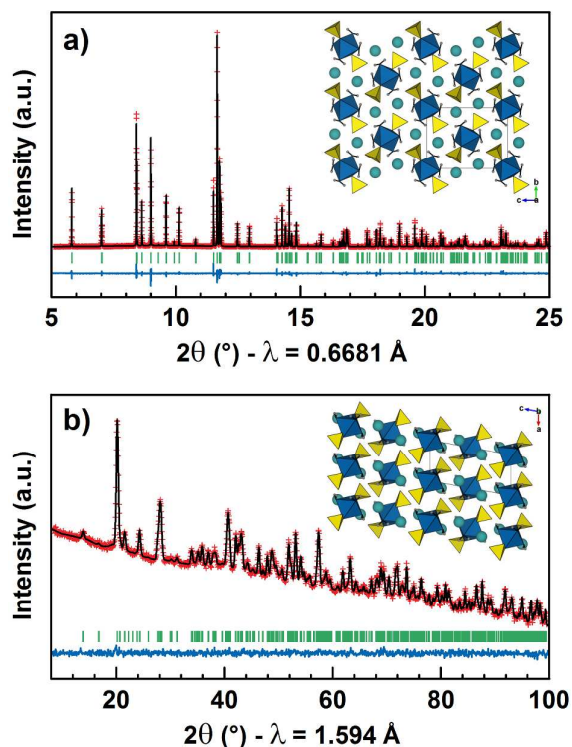
Figure 2:

Electrochemical characterization of $Na_2Fe(SO_4)_2.4H_2O$ (a) *versus* sodium and (b) *versus* lithium. On the left, typical voltage-composition traces show the flat-like first charge (in red) and the more sloping subsequent discharges and charges (blue to green). The corresponding derivative curves –dx/dV are displayed on the right. After the first charge (in red) which occurs at ~3.6 V *vs.* Na^+/Na^0 and ~3.8 V *vs.* Li^+/Li^0, the average potential is centered around 3.3 V *vs.* Na^+/Na^0 and 3.6 V *vs.* Li^+/Li^0 as indicated by the grey dotted lines in (a) and (b), respectively.
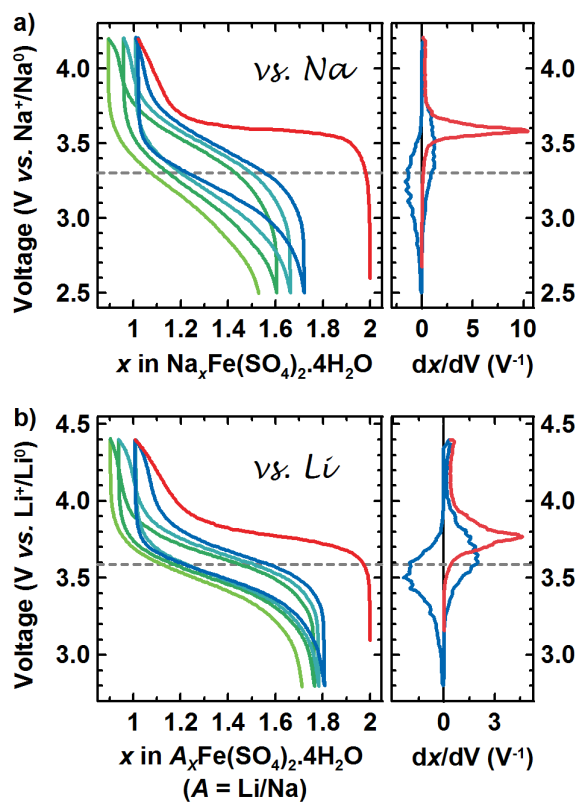
Figure 3:

(a) X-ray diffraction patterns at several compositions (x) of $Na_xFe(SO_4)_2.4H_2O$ samples prepared electrochemically. The star indicates a reflection of Be, due to the beryllium window which equipped our special XRD holder for air-sensitive samples. Note that the amorphization of the active material during the first charge is accompanied by a growth of the background in the range $20 \leq 2\theta \leq 45°$. (b) Mössbauer spectra of the pristine $Na_2Fe(SO_4)_2.4H_2O$ sample ($x = 2.0$; bottom), the sample at the end of the first charge ($x = 1.0$; middle) and the sample after the first discharge ($x = 1.7$; top).
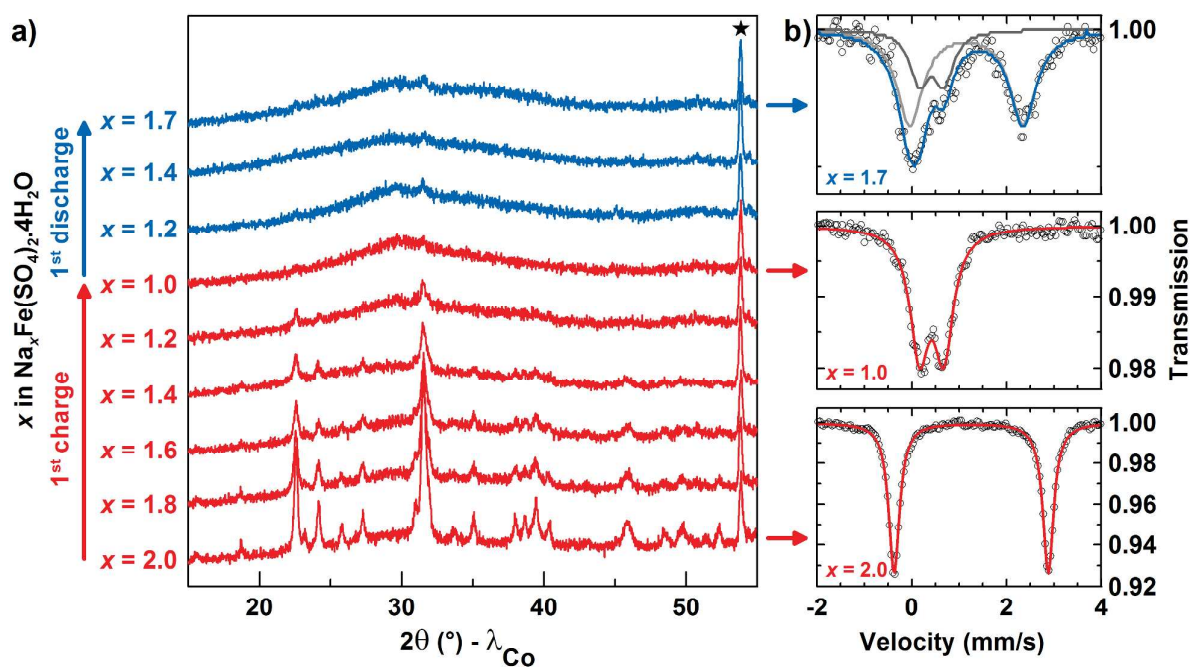
Figure 4:

Thermogravimetric analysis of $Na_2Fe(SO_4)_2.4H_2O$ (red line) and $Na_2Co(SO_4)_2.4H_2O$ (purple line) demonstrating the loss of four molecules of water between 110 and 250°C.
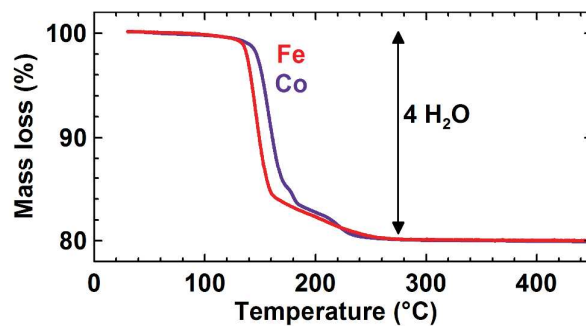
Figure 5:

Evolution of the XRD patterns upon the dehydration process of (a) $Na_2Fe(SO_4)_2 \cdot 4H_2O$ and (b) $Na_2Co(SO_4)_2 \cdot 4H_2O$. Blue patterns correspond to the $Na_2M(SO_4)_2 \cdot 4H_2O$ phases, green patterns to the intermediate step described in the text and red patterns to the α-$Na_2M(SO_4)_2$ phases.
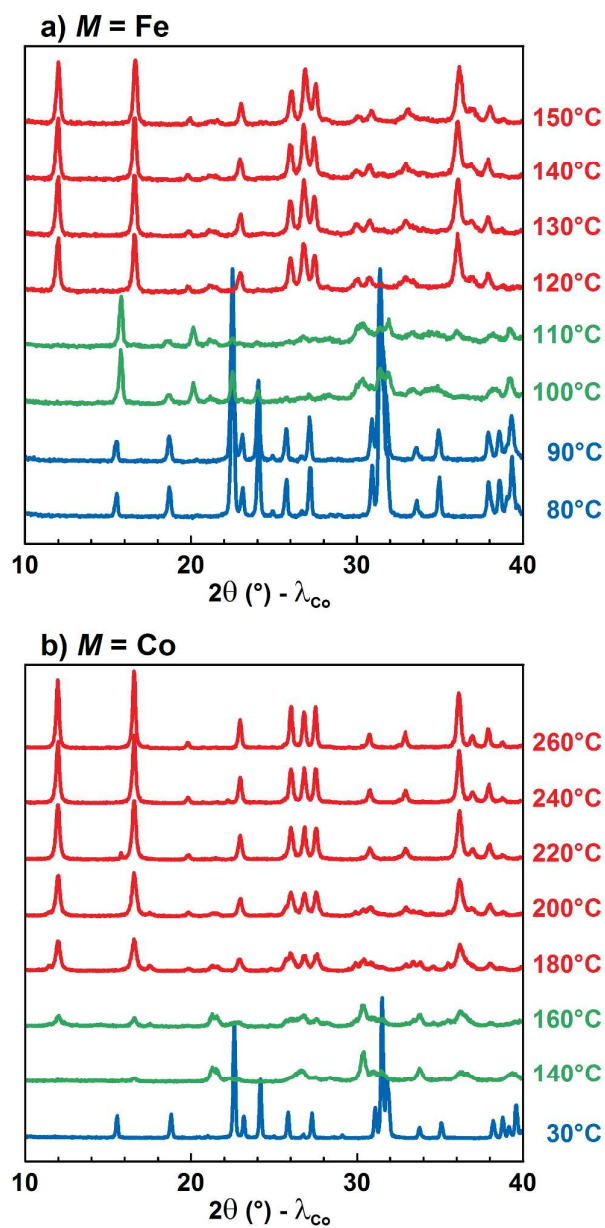
Figure 6:

(a) SAED patterns of α-Na$_2$Co(SO$_4$)$_2$ indexed in the monoclinic supercell as described in the text. (b) and (c) Results of the joint Rietveld refinement of the Synchrotron X-ray powder Diffraction and the Neutron Powder Diffraction patterns of α-Na$_2$Co(SO$_4$)$_2$ against this monoclinic supercell. The green ticks represent the Bragg peak positions of the phase, the red crosses and the black line are the experimental and the simulated patterns, respectively; the difference between these two patterns is shown with the blue line.
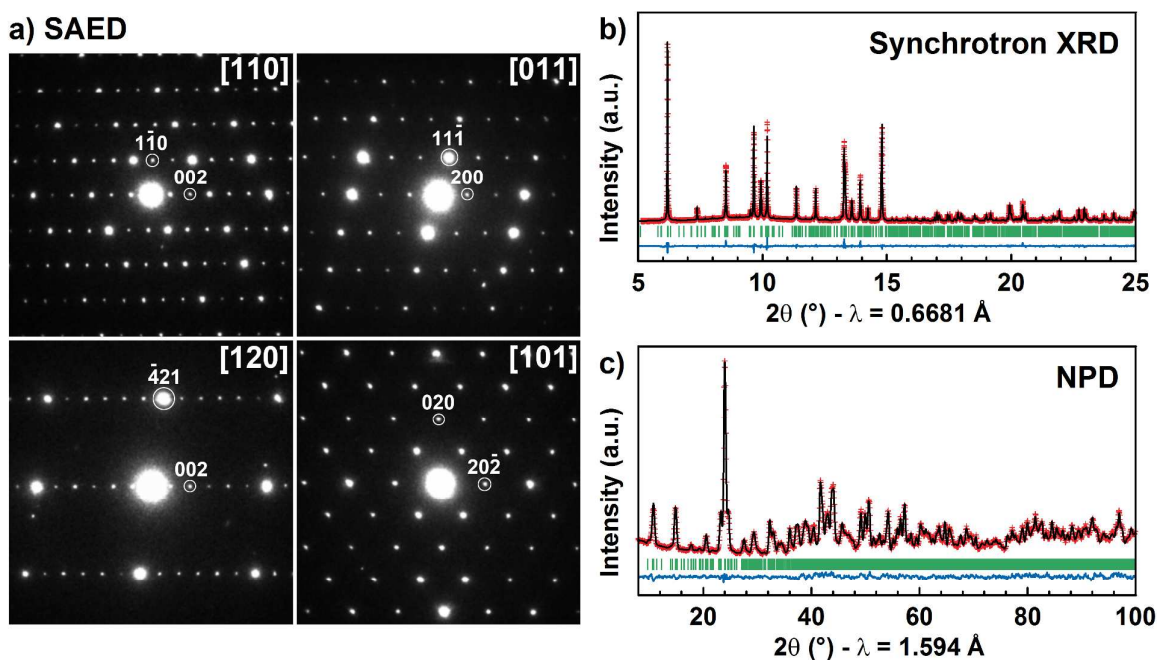
Figure 7:

Crystal structure of α-Na$_2$Co(SO$_4$)$_2$ represented with the monoclinic supercell described in the text. (a), (d) and (e) Projections along the *b*-axis, and the [1 0 $\bar{2}$] and [1 0 1] directions, respectively. CoO$_6$ and SO$_4$ groups are displayed as blue octahedra and yellow tetrahedra, respectively. Cyan spheres correspond to the sodium atoms. (b) Chains of CoO$_6$ octahedra and SO$_4$ tetrahedra, which are alternatively connected through corners and edges. Na atoms are not displayed for clarity. (c) Enlargement of one chain, where oxygen atoms are represented as small red balls and the edges shared by the CoO$_6$ octahedra and SO$_4$ tetrahedra are highlighted with red segments.
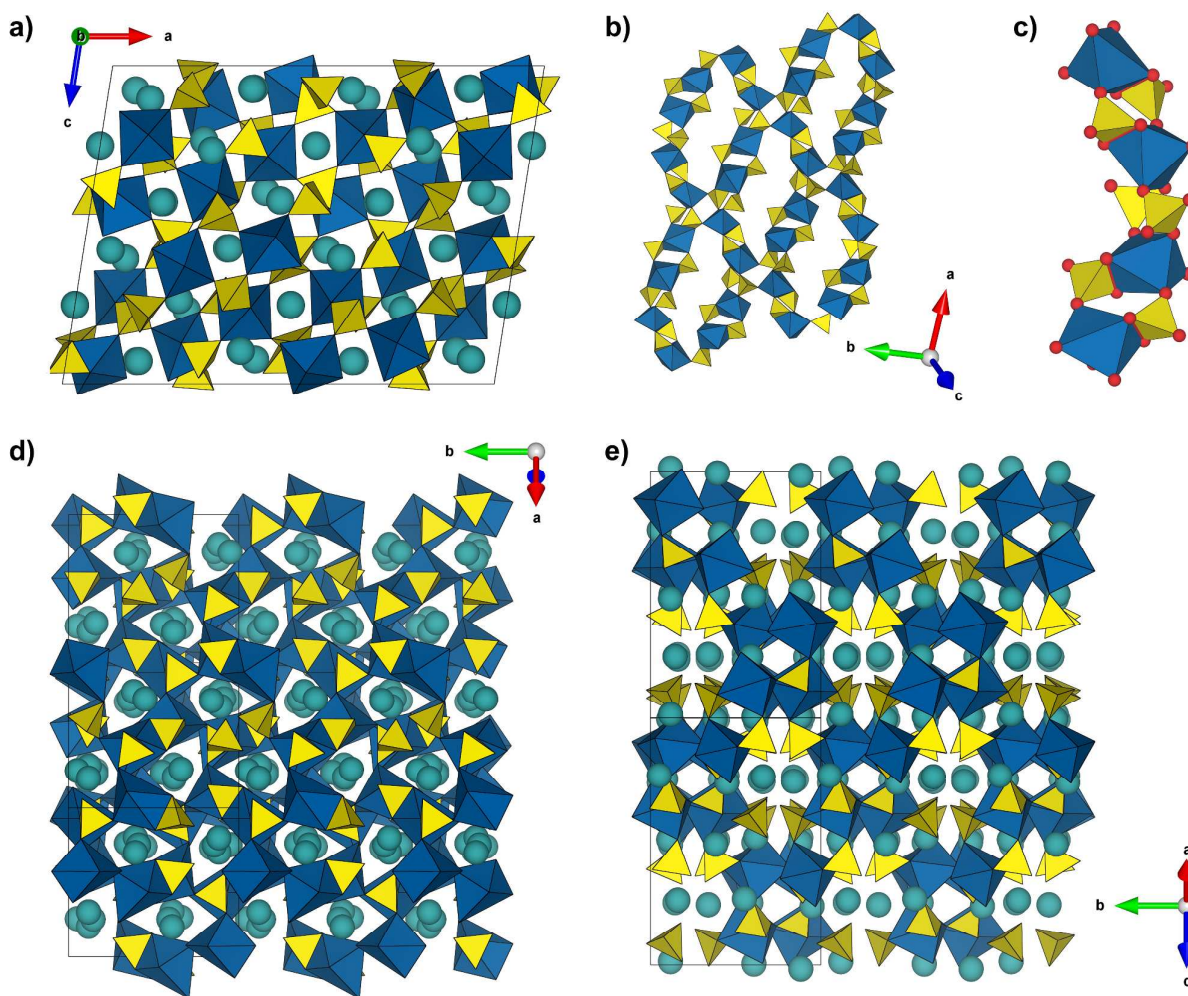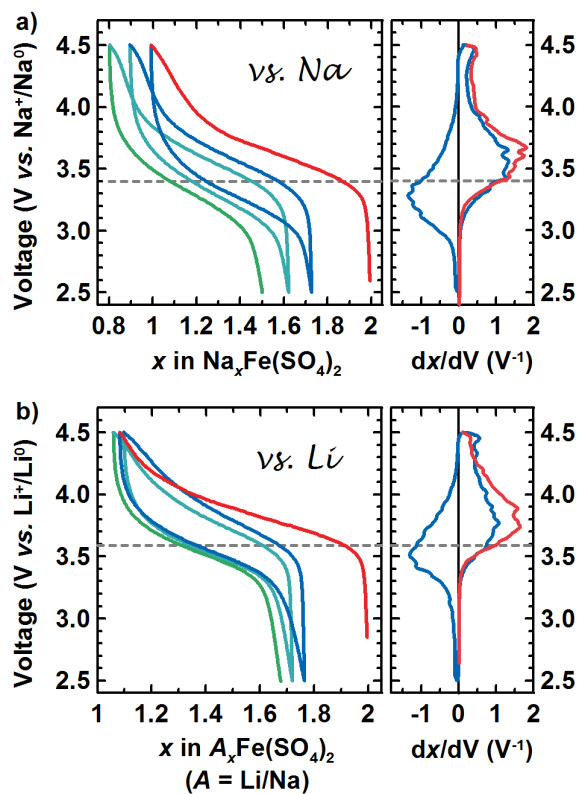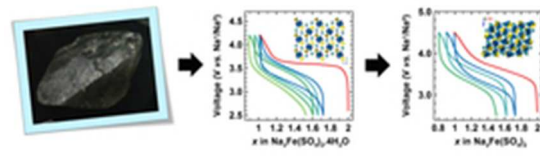
Figure 8:

Electrochemical characterization of α-Na$_2$Fe(SO$_4$)$_2$ (a) *versus* sodium and (b) *versus* lithium. The first charge is displayed in red and the subsequent discharges and charges are colored from blue to green. The corresponding derivative dx/dV curves are shown at the right part of the figure. Grey dotted lines indicate the average potential of (a) 3.4 V *vs.* Na$^+$/Na^0 and (b) 3.6 V *vs.* Li$^+$/Li^0.

23x6mm (300 x 300 DPI)